*Acta Oceanol. Sin.*, 2023, Vol. 42, No. 6, P. 24–32
https://doi.org/10.1007/s13131-022-2102-5
http://www.aosocean.com
E-mail: ocean2@hyxb.org.cn

# Detection and characteristics analysis of the western subarctic front using the high-resolution SST product

Changyuan Chen[1, 2], Chen Wang[1, 2*], Huimin Li[1, 2], Denghui Hu[3], Gang Li[1, 2], Xin Chen[1, 2], Yijun He[1, 2]

[1] School of Marine Sciences, Nanjing University of Information Science & Technology, Nanjing 210044, China

[2] Key Laboratory of Space Ocean Remote Sensing and Application, Ministry of Natural Resources, Beijing 100081, China

[3] Innovation Academy for Microsatellites, Chinese Academy of Sciences, Shanghai 201203, China

Received 5 June 2022; accepted 13 September 2022



**Abstract**

Oceanic front plays a significant role in the ocean vertical mixing and the regulation of air-sea interaction, among others. The western branch of the subarctic front (WSAF) located in the Northwest Pacific has attained lots of attention given its strong intensity and widespread influence on this region. In this study, we take advantage of the merged sea surface temperature (SST) at a high spatial resolution of 0.05° to investigate the characteristics of WSAF. The front detection algorithm that combines the Sobel operator and histogram analysis is adopted. It is advantageous in both preserving the front intensity represented by the SST gradient as well as reducing the detection noise level. We systematically applied this algorithm to the daily SST products for front detection, based on which the WSAF characteristics including its intensity, occurrence of frequency, latitudinal position and coverage area are then extracted. WSAF is mostly located within a small latitude range between 40°N and 41°N with a clear seasonal trend in its intensity that peaks in the winter and troughs in the summer. The seasonal variation of WSAF intensity is almost consistent throughout the temporal period of interest from 2010 to 2018. Similar seasonality is observed for its occurrence of frequency with the winter-summer contrast reaching up to 5%. The findings presented here shall help better interpret the WSAF characteristics in the long-term run as well as their impact on the regional weather and climate patterns at high spatial resolution.

**Key words:** sea surface temperature, western subarctic front, front detection, characteristics analysis

**Citation:** Chen Changyuan, Wang Chen, Li Huimin, Hu Denghui, Li Gang, Chen Xin, He Yijun. 2023. Detection and characteristics analysis of the western subarctic front using the high-resolution SST product. Acta Oceanologica Sinica, 42(6): 24–32, doi: 10.1007/s13131-022-2102-5

## 1 Introduction

Ocean front is a narrow zone where two water masses of high-gradient temperature and/or salinity meet (Kobashi et al., 2006; Belkin et al., 2009; Masujima and Yasuda, 2009; Yao et al., 2018). The subarctic front (SAF) is the permanent front in the Northwest Pacific, located around 40°N and formed by the intersection of the warm Kuroshio Extension and the cold Oyashio. SAF has significant impact on the local weather and regional climate due to the active air-sea interaction over this area (Sampe et al., 2010; Tomita et al., 2011; Yao et al., 2018). In general, SAF can be divided into two sub-regions, the western subarctic front (WSAF) between 146°E and 152°E, and the eastern subarctic front (ESAF) between 162°E and 171°E (Sugimoto et al., 2014; Yu et al., 2020; Zhu et al., 2019). By comparison, the WSAF branch exhibits much higher intensity and wider coverage relative to its eastern companion, whose characteristics are therefore much more often investigated.

The detection method of ocean fronts has experienced substantial changes over the last decades. Earlier efforts mostly rely on the *in-situ* observations, such as from the coastal stations, ship reporting, buoys and so on (Gordon, 1975; Nagata et al., 1988; Rintoul and England, 2002; Nakamura and Kazmin, 2003). These observatory manners are limited in space and time as well as vulnerable to the severe weather. They are thus not suitable for continuous data collection over a long time period and large area in support of the spatial and temporal study of ocean fronts. Benefiting from the technical development, satellite remote sensing has become one of the most effective and efficient measurement sources to observe sea surface temperature (SST). This is attributed to its advantages of consistent observations over the extended spatial and temporal scope (Guan and Kawamura, 2004; Dash et al., 2012; Xu et al., 2018). The accurate identification of ocean front using remote sensing data naturally becomes the primary task for the subsequent applications. Over the past decades, a number of methods have been proposed to detect the ocean front and most are based on the SST field (Cayula and Cornillon, 1992; Simhadri et al., 1998; Shaw and Vennell, 2000; Shimada et al., 2005; Chen, 2008; Kuang et al., 2012; Nakano et al., 2018). Given the computational efficiency as well as the detection accuracy, the histogram analysis and the gradient meth-

Foundation item: The Natural Science Foundation of Jiangsu Province under contract No. BK20210666; the National Natural Science Foundation of China under contract Nos 41620104003 and 42006163; the Startup Foundation for Introducing Talent of Nanjing University of Information Science & Technology; the National Key Research and Development Program of China under contract No. 2021YFB3901004; the Graduate Innovation Project of Jiangsu Province under contract No. KYCX21_0980.
*Corresponding author, E-mail: cwang@nuist.edu.cn

od are the most popular approaches (Wang et al., 2020). The former, proposed and applied for ocean front detection by Cayula and Cornillon (1992, 1995, 1996), makes use of the SST distribution to determine whether a front exists. While the latter identifies the front by applying a threshold to the SST gradient. Many gradient operators are utilized in the literature, from the simplest pixel difference (Yuan and Talley, 1996; Han et al., 2021; Yang et al., 2021) to the Sobel, Canny operator etc. Among them, the Sobel operator is advantageous in obtaining the noise-resisting gradient field at finer spatial scale (Davis, 1975; Zheng et al., 2020). While Canny is generally employed to identify the central line of the oceanic front where the largest SST gradient occurs (Ping et al., 2014). The spatial distribution and variation of ocean front characteristics over different regions have been studied based on the Canny detected results (Shao et al., 2015; Wang et al., 2020). Yet, it is worth noting that either the histogram analysis or gradient method has its own limitations. Ullman and Cornillon (2000) demonstrated that the gradient method is subject to a higher error rate, while the histogram has more missing fronts. A method combining the Canny and histogram analysis has recently been proposed (Kirches et al., 2016) by uniting the individual advantages of these two techniques, exhibiting much improved performance in detecting the ocean front.

Most of the previous studies on the ocean front detection in WSAF employ the gradient method. Based on the gridded climatological data, Yuan and Talley (1996) calculated the horizontal difference of 10 m depth temperature and analyzed the entire SAF structure. The long-term WSAF intensity variation is also investigated using the monthly SST dataset (Sugimoto et al., 2014) and daily products (Zhu et al., 2020), respectively. Note that the gradient method for front detection plus the coarse resolution of SST data (mostly at 0.25° by 0.25°) jointly result in the difficulties in identifying the small and weak fronts. In this study, we take advantage of the high-resolution SST dataset at 0.05° resolution with an adapted detection algorithm by combining the Sobel operator and histogram analysis to determine the ocean front features over WSAF (37°–45°N, 146°–152°E). This shall help resolve the smaller and weaker fronts, complementary to the previous studies. Benefitting from the long duration of the SST products from March 2010 to February 2019, the seasonal and annual variation of the WSAF characteristics including its intensity, occurrence of frequency, latitudinal location and coverage area are also addressed.

Remainder of this paper is organized as follows. Section 2 describes the high-resolution SST products and the combined algorithm for ocean front detection. Results and Discussion are presented in Section 3 with the Conclusions followed in Section 4.

## 2 Data and methods

### 2.1 *Data*

In this study, we utilize the reprocessed Operational Sea Surface Temperature and Sea Ice Analysis (OSTIA) SST products available within the framework of the Copernicus Marine Service. It provides a global, daily and gap-free SST field based on satellite and *in-situ* measurements at a spatial resolution of 0.05° (Donlon et al., 2012; Good et al., 2020). The dataset is publicly available via https://resources.marine.copernicus.eu/. To investigate the temporal variation of WSAF features, SST data between March 2010 and February 2019 are analyzed to maintain the data consistency. Figure 1a presents the averaged SST field with a clearly decreasing trend of SST from the south toward the north. The isothermal lines of 20℃ and 15℃ are 5° apart in latitude, while the lines of 15℃ and 10℃ are only 3° apart, indicating a higher gradient in the north.

Here, we concentrate on the region of interest (ROI) covering 37°N to 45°N and 146°E to 152°E as marked by the red rectangle in Fig. 1a. The seasonal average of the SST field over this ROI is given in Figs 1b–e. The seasonal variation is clear with low temperature in winter and high values in summer. Note that the WSAF roughly locates between the isothermal lines of 5℃ and 10℃ in Fig. 1b. Therefore, it can be speculated that the SST gradi-

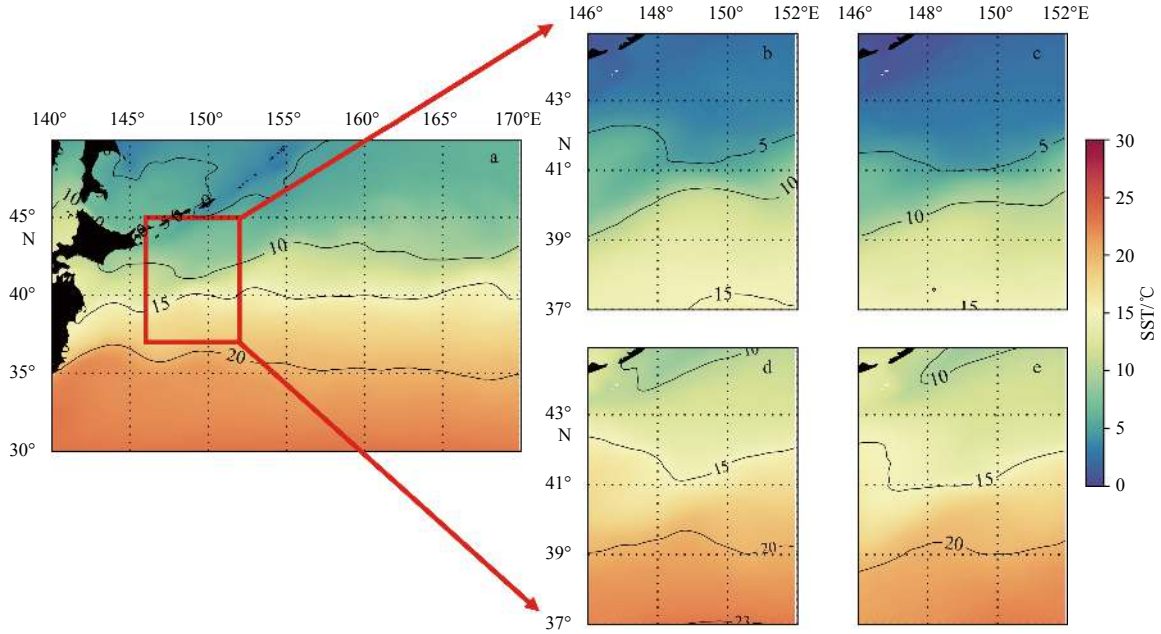


**Fig. 1.** The mean SST in the Northwest Pacific from March 2010 to February 2019 (a) and the seasonally averaged SST over the region of interest in winter (b), spring (c), summer (d), autumn (e). The isothermal lines at 5℃, 10℃, 15℃ and 20℃ are overlapped as black contours.

ent associated with the WSAF is strong in winter (December-January-February, DJF) and spring (March-April-May, MAM), while relatively weak in summer (June-July-August, JJA) and autumn (September-October-November, SON).

### 2.2 *Method*

The front detection algorithm used in this study is adapted from Kirches et al. (2016) by combining the Sobel operator rather than the Canny operator with the histogram analysis. The flowchart of this combined detection algorithm is shown in Fig. 2. It can be divided into three steps: the first is to calculate the SST gradient based on the Sobel operator, then to determine if there exists any ocean front within one window in terms of the SST histogram. The final step is to take the front presence as a filtering mask and apply it to the SST gradient. The characteristics of WSAF, including its intensity, frequency of occurrence, latitudinal position and coverage area are then accordingly estimated. In the following, we detail each step along with a case study shown in Fig. 3 to better illustrate the implementation process of this adapted front detection algorithm.

The first step is to calculate the SST gradient with the input example SST data given in Fig. 3a. In practice, we use the following 3×3 convolution operator in the longitudinal ($x$) and the latitudinal ($y$) direction to calculate the gradient, $\boldsymbol{G}_x$ and $\boldsymbol{G}_y$, respectively:

$$\boldsymbol{G}_x = \begin{bmatrix} -1 & 0 & 1 \\ -2 & 0 & 2 \\ -1 & 0 & 1 \end{bmatrix} \times \mathrm{SST}, \tag{1}$$

$$\boldsymbol{G}_y = \begin{bmatrix} -1 & -2 & -1 \\ 0 & 0 & 0 \\ 1 & 2 & 1 \end{bmatrix} \times \mathrm{SST}, \tag{2}$$

$$|\boldsymbol{G}| = \sqrt{\boldsymbol{G}_x^2 + \boldsymbol{G}_y^2}. \tag{3}$$

The SST gradient obtained by $\boldsymbol{G}_x$ and $\boldsymbol{G}_y$ are plotted in Figs 3b and c, respectively, with the magnitude $|\boldsymbol{G}|$ in Fig. 3d. As shown, the longitudinal gradient is small across most of the regions, while the features of latitudinal SST gradient in Fig. 3c are in alignment with the position of WSAF. This implies that the SST variation associated with WSAF is mostly along the north-south direction, which is further evidenced by the resembling Figs 3c and d.

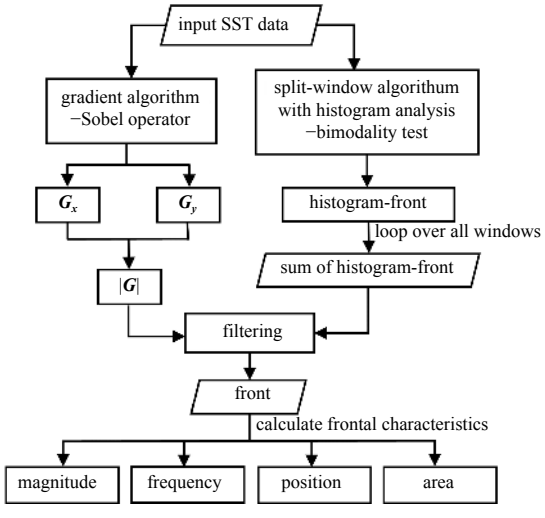


**Fig. 2.** Flowchart of the combined algorithm for front detection.

In the histogram analysis, the input SST matrix is divided into overlapping sub-windows of 11×11 pixels. The overlapping distance between sub-windows is set to be one pixel. Over each sub-window, the histogram of the SST field is computed with a fixed number of 30 bins and the bin size is thus automatically adjusted to the SST range. The presence of an ocean front within a sub-window is determined by the modality of the obtained histogram. The bimodal SST distribution as in Fig. 3f corresponds to the front existence and one single peak to no front (Fig. 3e). To lower the misdetection possibility, a peak is valid only when it outnumbers its adjacent 10 points. Such detection is completed by moving the sub-window over the entire ROI and the detected fronts are given in Fig. 3g. In this study, we also make use of the Canny algorithm (Ping et al., 2014) to extract the central line of ocean fronts. The high and low thresholds required for the Canny detection to mark the pixels whose values lie between as the front point are set at 0.009℃/km and 0.018℃/km, respectively. The overlapped front central lines in Fig. 3g illustrate good agreement between these two methods, further evidencing the validity of the histogram analysis.

Finally, the fronts are identified by taking the histogram results as a filtering mask and applying it to the SST gradient, as in Fig. 3h. Such detection is advantageous in that it not only reserves the strong gradient information which is aligned with the Canny front lines (black curves), but significantly reduces the noise. This combined algorithm is then systematically employed to determine the ocean front with the daily SST product over the ROI. Based on the detected results, the following variables associated with the WSAF characteristics are computed for the subsequent statistical analysis. The occurrence of frequency of ocean fronts at each pixel is defined as the ratio of the number marked as a front to the total number of observations (Xu et al., 2015). The area of ocean front is expressed as a product of the number of front pixels and the unit area of each pixel. The WSAF intensity is represented by the maximum SST gradient at its central location (latitude).

## 3 Results and discussion

In this section, the detected ocean fronts based on the combined algorithm are presented in terms of their gradient intensity, occurrence of frequency over the ROI as well as their seasonal variations. Temporal change of the WSAF characteristics over the period of 2010–2019 is also included.

### 3.1 *Spatial characteristics of WSAF*

Seasonal average of the SST gradient along with the detected ocean fronts is given in the top panel of Fig. 4. The SST gradient feature is strongly related to the WSAF pattern as it is a common representative of the front intensity. The pattern of high SST gradient marked in red runs along the northeast-southwest direction, which is in good agreement with the WSAF path as given in Zhu et al. (2020). Outside the WSAF influencing region, the SST gradient is much lower. The seasonal variation of SST gradient is also obvious. The WSAF intensity reaches its maximum during DJF as in Fig. 4a and decreases to its minimum in JJA in Fig. 4c, consistent with the results presented in Sugimoto et al. (2014) and Zhu et al. (2020). In addition to its intensity, the spatial extent of WSAF also varies with seasons, which is more clearly depicted by the solid SST gradient contour. The area circled by the contour of 0.023℃/km in winter is clearly larger than that

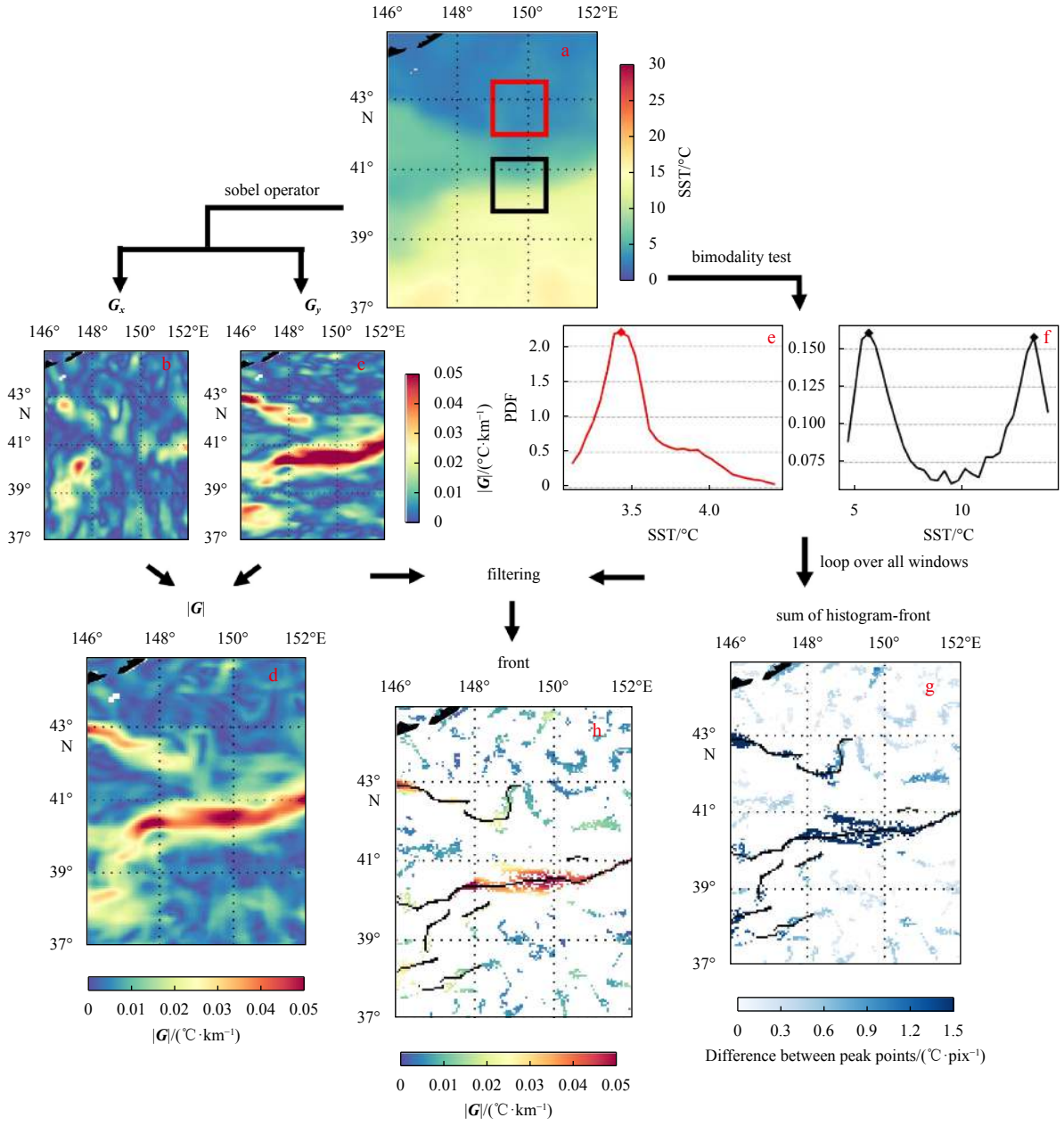


**Fig. 3.** An example of the combined detection algorithm used in this study. The input SST data (a), the longitudinal and latitudinal SST gradient (b, c), magnitude of the SST gradient (d). The probability density function (PDF) of SST data over the red (black) rectangle (e, f) in a, SST front detected by the histogram analysis (g) and the combined algorithm (h). The black curves in g and h denote the central front lines obtained by the Canny algorithm.

circled by 0.017℃/km in summer. Note that the small front located in the northwest corner of the ROI appears to have opposite trend in that both its intensity and spatial extent reach their peak in summer. As shown, this front extends to the east of 148°E in summer, while is bounded in the west during the wintertime.

The seasonal occurrence of frequency of detected ocean front is given in the bottom panel of Fig. 4. The overlapped contour represents the occurrence of frequency calculated by the percentage of SST gradient greater than 0.01℃/km. The location of frequent front is roughly consistent with that of high SST gradient. It mostly appears along the east-west direction with the maximum occurrence between 148°E and 150°E. The seasonal variation also conforms to the intensity plot that the high SST gradient corresponds to the high occurrence of frequency as in winter. The percentage obtained based on the combined algorithm in background color sees its maximum during DJF, reaching up to 25% and decreasing to around 18% during JJA across the WSAF path. By comparison, the smaller front located around 43°N and 146°E shows a minor seasonal change with steady percentage around 23%. It is worth pointing out here that the occurrence of frequency detected by the combined algorithm is much lower than that obtained based on the SST gradient. As a matter of fact, it is kind of expected given the excessive front misidentification using the simplified threshold of 0.01℃/km. This threshold is usually an empirical value and varies from one region to another, possibly resulting in the misassignment of a single pixel with higher SST gradient as ocean front. In contrast, the combined algorithm takes the surroundings of a given pixel to determine the

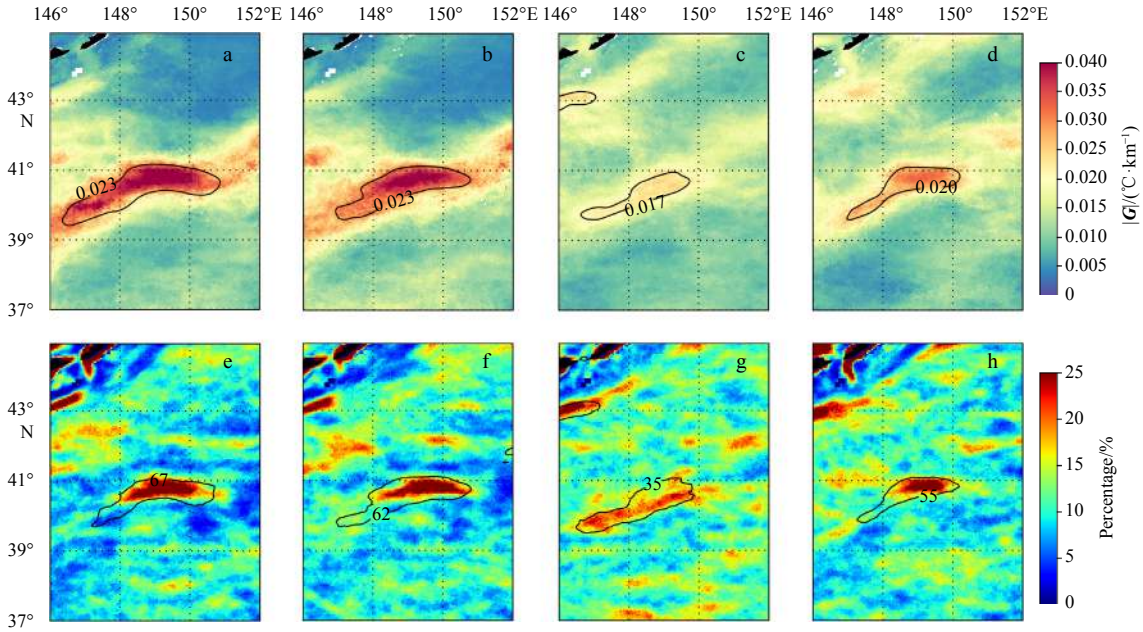


**Fig. 4.** Seasonal average of SST gradient and the occurrence of frequency over the detected ocean front by the combined algorithm in winter (DJF) (a, e), spring (MAM) (b, f), summer (JJA) (c, g) and autumn (SON) (d, h), respectively. The black contour in the bottom panel is the frequency of SST gradient larger than 0.01℃/km.

presence of front features. It, to a certain extent, lowers the false alarm rate of including single pixels, which is one of the advantages of this detection method.

Figure 5 displays the seasonal occurrence of frequency of central front line obtained using the Canny algorithm as described above. Similar to the results in Fig. 4, the high occurrence of ocean fronts mostly lies in the path of WSAF as well as south of the islands in the northwest corner of this ROI. These patterns persist throughout the year, reaching their maximum around 15% in DJF and down to the minimum about 9% in JJA. In comparison to the combined algorithm, the level of detected occurrence of frequency by Canny is generally lower by 10% across the four seasons. This could be attributed to the fact that the Canny operator only preserves the central line of ocean front while masking out the front influencing region. That is to say, such occurrence of frequency is representative of the percentage that each pixel positions in the central front line, which is different from the values in Fig. 4. The Canny results are therefore complementary to the combined algorithm to depict the occurrence of central front line.

### 3.2 *Temporal variation of WSAF*

As described in Section 2.2, the combined algorithm is applied to detect the ocean front, which generates a map of front intensity characterized by the SST gradient on a daily basis. We first look into the variation of the typical front intensity, represented by the percentile of SST gradient over the ROI. The monthly mean of four percentiles of 50th, 90th, 95th and 100th are chosen and given in Fig. 6. The SST percentile is the value below which a certain percentage of the data during that year is located. For example, the 90th percentile is the SST gradient where 90% of the data is below this value. Here, the monthly percentiles are obtained by averaging the percentile values of each day in that month. The median (50th percentile) is almost steady over time with weak seasonality, whose deviation is less than 0.005℃/km. While the other three percentiles exhibit a resembling variation with clear seasonality that the peak intensity appears in winter months and the trough in late summer. The magnitude of the increase in SST gradient from 50th to 90th is observed to vary with seasons. On average, a magnitude difference of about 0.01℃/km is found in summer and this value goes up to 0.03℃/km in the wintertime. This is mostly due to the seasonal variation of the

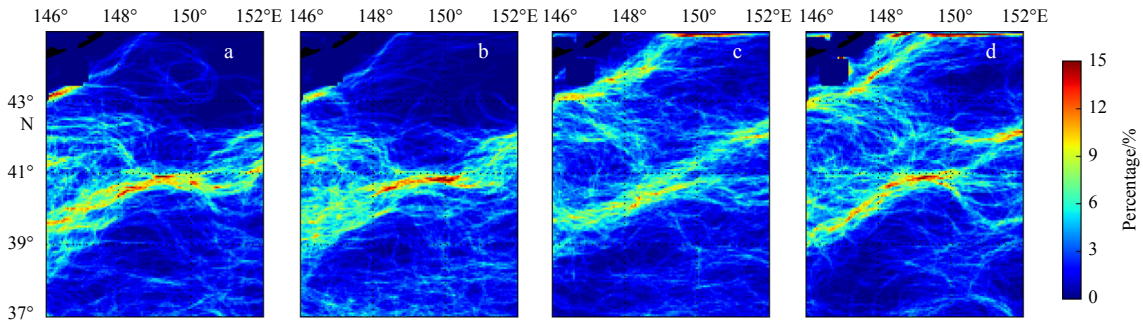


**Fig. 5.** Occurrence of frequency of central front line obtained by the Canny detection algorithm in winter (DJF) (a), spring (MAM) (b), summer (JJA) (c) and autumn (SON) (d).

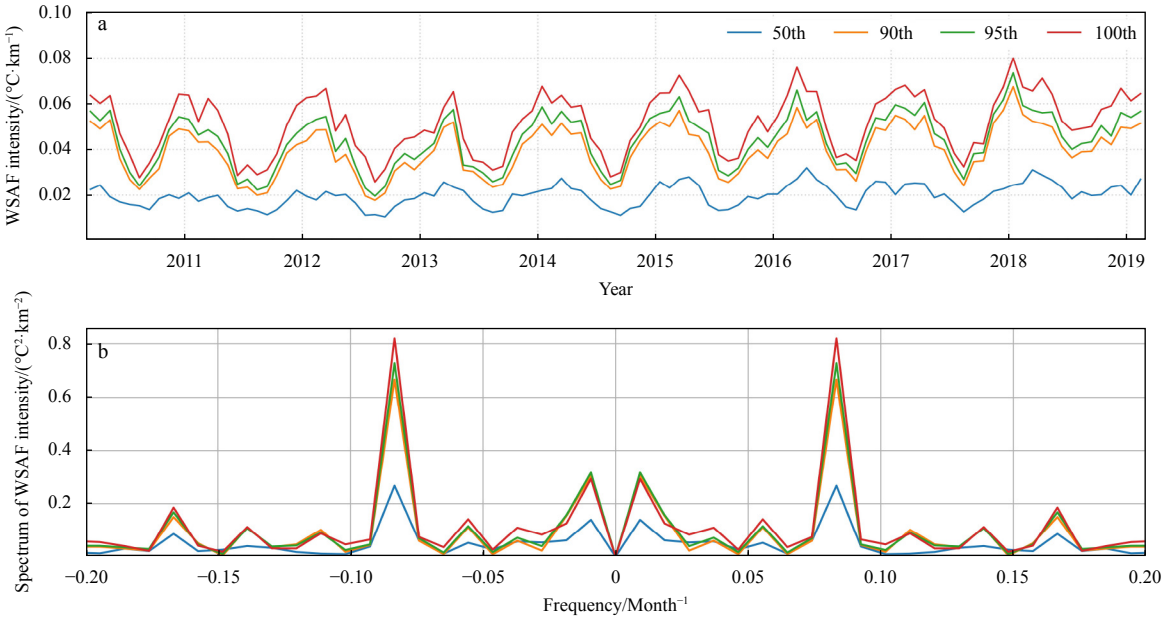


**Fig. 6.** The monthly mean of different SST gradient percentile of 50th (blue), 90th (orange), 95th (green) and 100th (red), respectively (a); spectrum magnitude of the monthly percentiles (b). WSAF: western branch of the subarctic front.

90th. In addition, the result of 95th is much closer to 90th than it is to 100th. Accordingly, the seasonal variation of the 100th percentile, namely the maximum gradient, shows the most distinct trend with the deviation larger than 0.03℃/km. This lays the basis for the subsequent analyses of using the 100th percentile or the maximum gradient as a representative descriptor for the WSAF intensity. We also calculated the power spectrum of these percentile signal to quantify their temporal period as presented in the bottom panel of Fig. 6. The maximum magnitude is observed at 12 months, implying a strong yearly cycle. It is worth noting that the 50th exhibits the lowest spectrum and the other three percentiles show comparable magnitude, which is consistent with the yearly variations.

The temporal variation of WSAF intensity spanning 2010–2019 is plotted in Fig. 7a with the curves in colors representing the daily intensity in different seasons and the solid black being the monthly average. The seasonal trend of the WSAF intensity is fairly obvious that the front has the strongest intensity in later winter and the weakest in later summer, which is consistent with the pattern shown in Fig. 4. It should be pointed out that the curve of monthly average is essentially the same as that of the 100th percentile in Fig. 6. In addition, the daily WSAF intensity manifests a certain variability within one given season, such as in the summer of 2010 where a quite strong WSAF intensity is observed across several days. This is possibly due to either an abnormal disturbance of the front by other geophysical processes

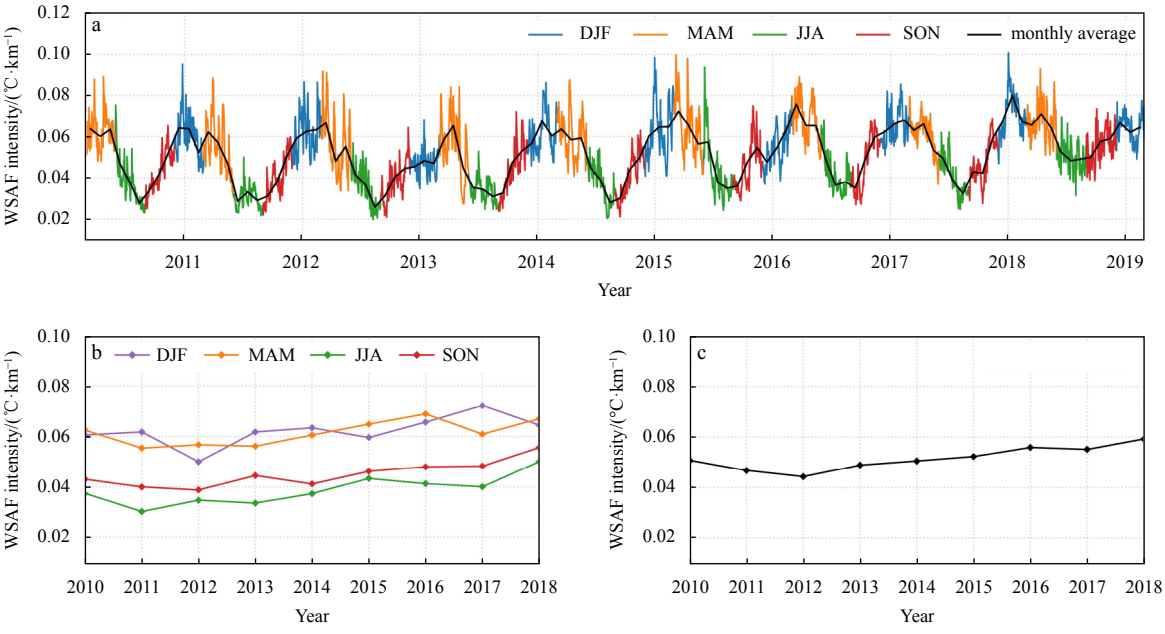


**Fig. 7.** Temporal variation of the daily western branch of the subarctic front (WSAF) intensity obtained by the combined algorithm (a), the seasonal intensity (b) and the annual intensity (c).

or the anomalous SST products acquired by the individual sensors during these days. Nevertheless, such kind of outliers are expected not to influence the seasonal trend of WSAF intensity as given in Fig. 7b. The front intensities in winter (DJF) and spring (MAM) are generally stronger than those in the other seasons roughly by 0.02℃/km, while winter and spring alternatively take the lead across this time span of interest and so are the summer and autumn. In addition, it is surprising that the seasonal average presents an overall increasing trend from 2010 onwards. The annual average of WSAF intensity in Fig. 7c depicts such variation more straightforwardly, particularly from 2012 to 2016. Despite an increasing trend, it might be associated with a normal oscillation of WSAF intensity. Given the relatively short period of SST products included in this study, we are not yet able to conclude a valid strengthening in the WSAF intensity, which is also beyond the scope of this paper. This aspect shall be expected to be investigated elsewhere in the future based on a long-term data set (at least 30 years). It should be mentioned that the WSAF intensity obtained in this study is slightly higher than that reported in Zhu et al. (2020). This might be attributed to the fact that the SST data at 25 km used in Zhu et al. (2020) is much smoother, leading to a lower gradient.

As presented above, the WSAF intensity described by the maximum SST gradient shows a strong seasonality. Variation of the WSAF latitudinal location determined by the position where the maximum SST gradient occurs is given in Fig. 8. It should be noted that only the meridional component is examined on account of the quasi permanent existence of WSAF across the ROI. The averaged SST gradient over [148°E, 150°E] is overlapped as the background color to help interpret the WSAF location. The daily WSAF location (blue curve) exhibits a slightly seasonal signal that the WSAF is mostly located around the latitude of 40°N during the wintertime and moves northward to around 41°N in the summer. In terms of the monthly mean (solid black curve) and median curve (dashed red), the WSAF position determined by the location of maximum SST gradient mostly varies within a latitude range of 1°, which is consistent with the previous results reported in Sugimoto et al. (2014) and Zhu et al. (2020). It is also worth noting that the WSAF reaches as far north as 42°N in the summer of 2014 and is located much further north than the previous years, which might be driven by the large-scale climate process, such as El Niño. The exact reason is yet necessary to be further explored based on long-term data series as discussed later.

Taking advantage of the high-resolution SST product at 0.05°, the estimate of total area that could be assigned as the front influencing region becomes more accurate. Given the small ROI examined in this study, the grid size variation relative to the latitude is not considered for simplicity with the unit area of each point being 30.8 km$^2$. It is worth mentioning here that the WSAF front influencing region is determined by the combined algorithm across the latitudes of 39°–42°N, which is displayed in Fig. 9. The monthly average is plotted by the black curve. As such, this region includes 7 200 grids with the total area of 221 760 km$^2$. The averaged area of WSAF over the entire period is 24 749.41 km$^2$, accounting for 11.16% of the total area. The seasonality in the year of 2010, 2012 and 2018 is much evident, reaching maximum in the summer and the low point in the winter. By comparison, the seasonal variation is relatively small in the rest of time under study. Note that the WSAF coverage area based on the combined algorithm is expected to be smaller than using a simplified threshold for front detection.

## 4 Conclusions

WSAF is the quasi permanent front located in the Northwest

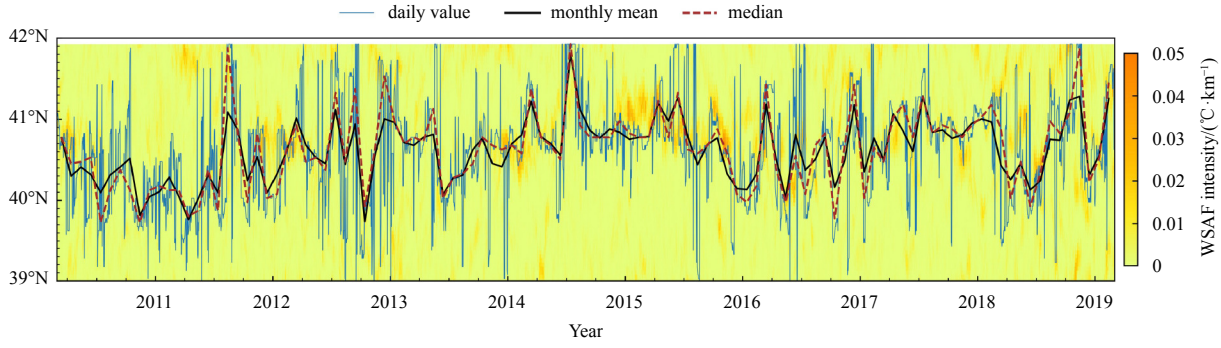


**Fig. 8.** Time series of the western branch of the subarctic front (WSAF) location on a daily basis (blue line). The monthly mean and median are plotted in solid black and dashed red, respectively. The background color represents the averaged SST gradient between 148°E and 150°E.

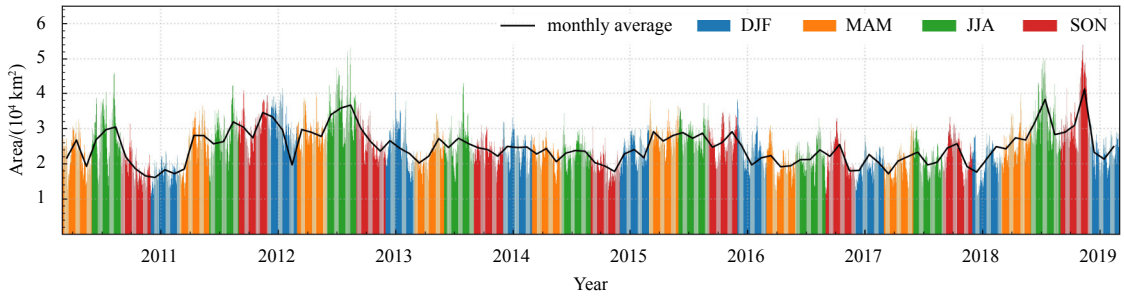


**Fig. 9.** Temporal variation of the western branch of the subarctic front (WSAF) area detected by the combined algorithm. Bars are the daily area color coded by seasons and the black curve is the monthly average. DJF: winter; MAM: spring; JJA: summer; SON: autumn.

Pacific, which makes it an ideal test bed for the front detection method as well as the analyses of its characteristics. In this study, we adapted a front detection algorithm by combining the Sobel operator and histogram analysis on the basis of Kirches et al. (2016) and systematically applied it to the high-resolution SST products. This algorithm is advantageous in that the front intensity could be accordingly represented by the obtained SST gradient in addition to the lower misdetection rate and the reduced noise level. Much finer-scale fronts are identified in comparison to the previous studies, which allows a thorough investigation of the WSAF characteristics.

Based on the front detection results from the combined algorithm, the variation of front intensity and the occurrence of frequency at spatial scope are addressed over the ROI (37°–45°N, 146°–152°E). First of all, the WSAF path is clearly pictured by the higher SST gradient, whose location shows a minor seasonal variation. And the WSAF intensity exhibits a strong seasonality with the peak appearing in wintertime and the weakest in the summer. A similar pattern is observed for the occurrence of frequency with the highest frequency in winter. These trends are consistent with the previously reported results (Sugimoto et al., 2014; Zhu et al., 2020), but at finer spatial scale. The WSAF intensity represented by the maximum SST gradient over the WSAF influencing region is also explored. The seasonal signal is evident with the winter-summer difference reaching up to 0.03℃/km. Over the temporal period under study, the averaged WSAF intensity presents a slightly increasing trend. Yet, we are not in the position to affirmatively conclude it given the 10-year duration of SST products included in this study. In addition, the high spatial resolution of SST products makes the estimate of WSAF coverage area more accurate in comparison to the previous studies based on the SST field at 0.25° grids.

It has been well recognized that WSAF is significant to the regional weather, climate and ecosystems. Its characteristics are expected to modulate these physical processes via the air-sea interaction and the ocean mixing, among others. The increasingly improved SST dataset enables us to resolve the WSAF features at finer scales and details. For example, the occurrence of frequency obtained in this study based on the combined algorithm and the high-resolution SST dataset is larger than that reported previously (Wang et al., 2020). This might be due to the fact that our detection results include more front features that could not be identified using the SST product at 0.25°. As such, it is complementary to examine the long-term variability of WSAF characteristics based on the detection method employed here, which is beyond the scope of this paper but will be addressed in the near future. It will also facilitate the study of WSAF influence on the regional atmosphere-ocean interaction in the long-term perspective. Furthermore, SST assets at higher spatial and temporal resolution shall enable the detection of small-scale fronts, which are rapidly evolving processes that are currently yet difficult to be resolved. Such expanded front scope from large-scale to small-scale shall allow far more in-depth investigation of the WSAF and other front features worldwide.

***Acknowledgements***

The authors want to acknowledge the High Performance Computing Center of Nanjing University of Information Science & Technology for their support of this work. We also thank the reviewers for their constructive comments which improves the paper.

**References**

Belkin I M, Cornillon P C, Sherman K. 2009. Fronts in large marine ecosystems. Progress in Oceanography, 81(1–4): 223–236

Cayula J F, Cornillon P. 1992. Edge detection algorithm for SST images. Journal of Atmospheric and Oceanic Technology, 9(1): 67–80, doi: 10.1175/1520-0426(1992)009<0067:EDAFSI>2.0.CO;2

Cayula J F, Cornillon P. 1995. Multi-image edge detection for SST images. Journal of Atmospheric and Oceanic Technology, 12(4): 821–829, doi: 10.1175/1520-0426(1995)012<0821:MIEDFS>2.0.CO;2

Cayula J F, Cornillon P. 1996. Cloud detection from a sequence of SST images. Remote Sensing of Environment, 55(1): 80–88, doi: 10.1016/0034-4257(95)00199-9

Chen Shuiming. 2008. The Kuroshio Extension Front from satellite sea surface temperature measurements. Journal of Oceanography, 64(6): 891–897, doi: 10.1007/s10872-008-0073-6

Davis L S. 1975. A survey of edge detection techniques. Computer Graphics and Image Processing, 4(3): 248–270, doi: 10.1016/0146-664X(75)90012-X

Donlon C J, Martin M, Stark J, et al. 2012. The operational sea surface temperature and sea ice analysis (OSTIA) system. Remote Sensing of Environment, 116: 140–158, doi: 10.1016/j.rse.2010.10.017

Good S, Fiedler E, Mao C Y, et al. 2020. The current configuration of the OSTIA system for operational production of foundation sea surface temperature and ice concentration analyses. Remote Sensing, 12(4): 720, doi: 10.3390/rs12040720

Gordon A L. 1975. An Antarctic oceanographic section along 170°E. Deep-Sea Research and Oceanographic Abstracts, 22(6): 357–377, doi: 10.1016/0011-7471(75)90060-1

Guan Lei, Kawamura H. 2004. Merging satellite infrared and microwave SSTs: methodology and evaluation of the new SST. Journal of Oceanography, 60(5): 905–912, doi: 10.1007/s10872-005-5782-5

Han Yansong, Zhang Lu, Qiao Lulu, et al. 2021. Multi-time scale variation of suspended sediment concentration over the eastern Shandong Peninsula under ocean front. Acta Sedimentologica Sinica (in Chinese), 41(3): 778–790

Kirches G, Paperin M, Klein H, et al. 2016. GRADHIST—A method for detection and analysis of oceanic fronts from remote sensing data. Remote Sensing of Environment, 181: 264–280, doi: 10.1016/j.rse.2016.04.009

Kobashi F, Mitsudera H, Xie Shangping. 2006. Three subtropical fronts in the North Pacific: observational evidence for mode water-induced subsurface frontogenesis. Journal of Geophysical Research: Oceans, 111(C9): C09033

Kuang Hailan, Perrie W, Chen Wei, et al. 2012. Thermal front retreivals from SAR imagery. In: Proceedings of 2012 IEEE International Geoscience and Remote Sensing Symposium. Munich: IEEE, 2637–2640

Masujima M, Yasuda I. 2009. Distribution and modification of North Pacific intermediate water around the subarctic frontal zone east of 150°E. Journal of Physical Oceanography, 39(6): 1462–1474, doi: 10.1175/2008JPO3919.1

Nagata Y, Michida Y, Umimura Y. 1988. Variation of positions and structures of the oceanic fronts in the Indian Ocean sector of the Southern Ocean in the period from 1965 to 1987. In: Sahrhage D, ed. Antarctic Ocean and Resources Variability. Berlin, Heidelberg: Springer, 92–98

Nakamura H, Kazmin A S. 2003. Decadal changes in the North Pacific oceanic frontal zones as revealed in ship and satellite observations. Journal of Geophysical Research: Oceans, 108(C3): 3078, doi: 10.1029/1999JC000085

Nakano H, Tsujino H, Sakamoto K, et al. 2018. Identification of the fronts from the Kuroshio extension to the subarctic current using absolute dynamic topographies in satellite altimetry products. Journal of Oceanography, 74(4): 393–420, doi: 10.1007/s10872-018-0470-4

Ping Bo, Su Fenzhen, Meng Yunshan, et al. 2014. A model of sea surface temperature front detection based on a threshold interval. Acta Oceanologica Sinica, 33(7): 65–71, doi: 10.1007/s13131-014-0502-x

Rintoul S R, England M H. 2002. Ekman transport dominates local air-sea fluxes in driving variability of subantarctic mode water. Journal of Physical Oceanography, 32(5): 1308–1321, doi: 10.1175/1520-0485(2002)032<1308:ETDLAS>2.0.CO;2

Sampe T, Nakamura H, Goto A, et al. 2010. Significance of a midlatitude SST frontal zone in the formation of a storm track and an eddy-driven westerly jet. Journal of Climate, 23(7): 1793–1814, doi: 10.1175/2009JCLI3163.1

Shao Lianjun, Zhang Honglei, Zhang Chunhua, et al. 2015. A method for detecting the oceanic front using remotely sensed sea-surface temperature. Hydrographic Surveying and Charting (in Chinese), 35(2): 42–44, 51

Shaw A G P, Vennell R. 2000. A front-following algorithm for AVHRR SST imagery. Remote Sensing of Environment, 72(3): 317–327, doi: 10.1016/S0034-4257(99)00108-X

Shimada T, Sakaida F, Kawamura H, et al. 2005. Application of an edge detection method to satellite images for distinguishing sea surface temperature fronts near the Japanese coast. Remote Sensing of Environment, 98(1): 21–34, doi: 10.1016/j.rse.2005.05.018

Simhadri K K, Iyengar S S, Holyer R J, et al. 1998. Wavelet-based feature extraction from oceanographic images. IEEE Transactions on Geoscience and Remote Sensing, 36(3): 767–778, doi: 10.1109/36.673670

Sugimoto S, Kobayashi N, Hanawa K. 2014. Quasi-decadal variation in intensity of the western part of the winter subarctic SST front in the western North Pacific: the influence of Kuroshio extension path state. Journal of Physical Oceanography, 44(10): 2753–2762, doi: 10.1175/JPO-D-13-0265.1

Tomita H, Kouketsu S, Oka E, et al. 2011. Locally enhanced wintertime air-sea interaction and deep oceanic mixed layer formation associated with the subarctic front in the North Pacific. Geophysical Research Letters, 38(24): L24607

Ullman D S, Cornillon P C. 2000. Evaluation of front detection methods for satellite-derived SST data using *in situ* observations. Journal of Atmospheric and Oceanic Technology, 17(12): 1667–1675, doi: 10.1175/1520-0426(2000)017<1667:EOFDMF>2.0.CO;2

Wang Yu, Yu Yi, Zhang Yang, et al. 2020. Distribution and variability of sea surface temperature fronts in the South China Sea. Estuarine, Coastal and Shelf Science, 240: 106793

Xu Suqin, Chen Biao, Tao Ronghua, et al. 2015. The temporal and spatial distribution characteristics of thermal front in the China seas. Journal of Telemetry, Tracking and Command (in Chinese), 36(3): 62–69, 74

Xu Bin, Yu Jingjing, Zhang Lei, et al. 2018. Research progress of global sea surface temperature fusion. Advances in Meteorological Science and Technology (in Chinese), 8(1): 164–170

Yang Yanlong, Liu Na, Fang Yue, et al. 2021. Spatial distribution and seasonal variation of ocean fronts in the sea of Japan. Advances in Marine Science (in Chinese), 39(3): 379–392

Yao Yao, Zhong Zhong, Yang Xiuqun. 2018. Impacts of the subarctic frontal zone on the North Pacific storm track in the cold season: an observational study. International Journal of Climatology, 38(5): 2554–2564, doi: 10.1002/joc.5429

Yu Peilong, Zhang Lifeng, Liu Mingyang, et al. 2020. A comparison of the strength and position variability of the Kuroshio Extension SST front. Acta Oceanologica Sinica, 39(5): 26–34, doi: 10.1007/s13131-020-1567-3

Yuan Xiaojun, Talley L D. 1996. The subarctic frontal zone in the North Pacific: characteristics of frontal structure from climatological data and synoptic surveys. Journal of Geophysical Research: Oceans, 101(C7): 16491–16508, doi: 10.1029/96JC01249

Zheng Huanhuan, Bai Yuxiu, Zhang Yaqiong. 2020. An edge detection algorithm based on Sobel operator. Microcomputer Applications (in Chinese), 36(10): 4–6

Zhu Kelan, Chen Xi, Mao Kefeng, et al. 2019. Mixing characteristics of the subarctic front in the Kuroshio-Oyashio confluence region. Oceanologia, 61(1): 103–113, doi: 10.1016/j.oceano.2018.07.004

Zhu Kelan, Chen Xi, Mao Kefeng, et al. 2020. Analysis on seasonal and interannual variations of the western Subarctic Front. Marine Science Bulletin (in Chinese), 39(1): 86–93